Monthly Notices
of the
ROYAL ASTRONOMICAL SOCIETY

MNRAS **528,** 5730–5741 (2024) https://doi.org/10.1093/mnras/stae033
Advance Access publication 2024 January 8

Discovery of radio eclipses from 4FGL J1646.5−4406: a new candidate redback pulsar binary

Andrew Zic [1]★ Ziteng Wang [2,3]★ Emil Lenc [1] David L. Kaplan [4] Tara Murphy [2,5]
A. Ridolfi [6,7] Rahul Sengar [4] Natasha Hurley-Walker,[3] Dougal Dobie [5,8] James K. Leung [1,2,5]
Joshua Pritchard [1,2,5] and Yuanming Wang [5,8]

[1]Australia Telescope National Facility, CSIRO, Space and Astronomy, PO Box 76, Epping, NSW 1710, Australia
[2]Sydney Institute for Astronomy, School of Physics, University of Sydney, Sydney, NSW 2006, Australia
[3]International Centre for Radio Astronomy Research, Curtin University, Bentley, WA 6102, Australia
[4]Center for Gravitation, Cosmology, and Astrophysics, Department of Physics, University of Wisconsin-Milwaukee, PO Box 413, Milwaukee, WI 53201, USA
[5]ARC Centre of Excellence for Gravitational Wave Discovery (OzGrav), Hawthorn, VIC 3122, Australia
[6]INAF – Osservatorio Astronomico di Cagliari, Via della Scienza 5, I-09047 Selargius (CA), Italy
[7]Max-Planck Institut fur Radioastronomie, Auf dem Hügel 69, D-53121 Bonn, Germany
[8]Centre for Astrophysics and Supercomputing, Swinburne University of Technology, Hawthorn, VIC 3122 ,Australia

Accepted 2023 December 20. Received 2023 November 21; in original form 2023 September 25

ABSTRACT

Large widefield surveys make possible the serendipitous discovery of rare subclasses of pulsars. One such class are 'spider'-type pulsar binaries, comprised of a pulsar in a compact orbit with a low-mass (sub)stellar companion. In a search for circularly polarized radio sources in Australian Square Kilometre Array Pathfinder (ASKAP) Pilot Survey observations, we discovered highly variable and circularly polarized emission from a radio source within the error region of the γ-ray source 4FGL J1646.5−4406. The variability is consistent with the eclipse of a compact, steep-spectrum source behind ablated material from a companion in an ∼5.3 h binary orbit. Based on the eclipse properties and spatial coincidence with 4FGL J1646.5−4406, we argue that the source is likely a recycled pulsar in a 'redback' binary system. Using properties of the eclipses from ASKAP and Murchison Widefield Array observations, we provide broad constraints on the properties of the eclipse medium. We identified a potential optical/infrared counterpart in archival data consistent with a variable low-mass star. Using the Parkes radio telescope 'Murriyang' and the Meer Karoo Array Telescope (MeerKAT) , we searched extensively for radio pulsations but yielded no viable detections of pulsed emission. We suggest that the non-detection of pulses is due to scattering in the intra-binary material, but scattering from the interstellar medium can also plausibly explain the pulse non-detections if the interstellar dispersion measure exceeds ∼600 pc cm^{-3}. Orbital constraints derived from optical observations of the counterpart would be highly valuable for future γ-ray pulsation searches, which may confirm the source nature as a pulsar.

Key words: binaries: eclipsing – pulsars: general – radio continuum: transients.

1 INTRODUCTION

Millisecond pulsars (MSPs; periods <30 ms) are excellent tools for a range of astrophysical applications, including stringent tests of general relativity (Kramer et al. 2021), studying the equation of state for neutron degenerate matter (Miller et al. 2019), searches for nanohertz-frequency gravitational waves (Agazie et al. 2023; EPTA Collaboration & InPTA Collaboration 2023; Reardon et al. 2023; Xu et al. 2023), and studying binary evolution (Benvenuto, De Vito & Horvath 2012; Chen et al. 2013; Smedley et al. 2015). They are formed after accreting matter from a companion star and spinning up to millisecond spin periods (Alpar et al. 1982), after which they are typically found in binary orbits with periods $P_{\rm b} \gtrsim 0.5$ d with their donor companions (Tauris & van den Heuvel 2006), though several isolated MSPs also exist.

'Spiders' are a rare class of MSP binary systems in which material from a low-mass companion in a compact orbit ($P_{\rm b} < 1$ d) is ablated by the relativistic pulsar wind (Roberts 2013). Spiders are comprised of two subclasses, known as 'black widows' with degenerate companions with masses ∼0.01–0.05 M$_{\odot}$, and 'redbacks' with main-sequence companions with masses >0.1 M$_{\odot}$ (Roberts 2013). The ablated companion material often causes radio eclipses, which occur due to enhanced dispersion, scattering, or absorption (Fruchter, Stinebring & Taylor 1988; Stappers et al. 1996; Polzin et al. 2020; Wang et al. 2021b; Bai et al. 2022).

Spiders likely represent very early stages in the life cycle of recycled pulsars (Benvenuto, De Vito & Horvath 2014), after the neutron star has completed accretion from the donor star. This is supported by the observation of multiple 'transitional' MSPs, which switch between a radio-pulsar mode and a low-mass X-ray binary (LMXB)

★ E-mail: andrew.zic@csiro.au (AZ); ziteng.wang@curtin.edu.au (ZW)

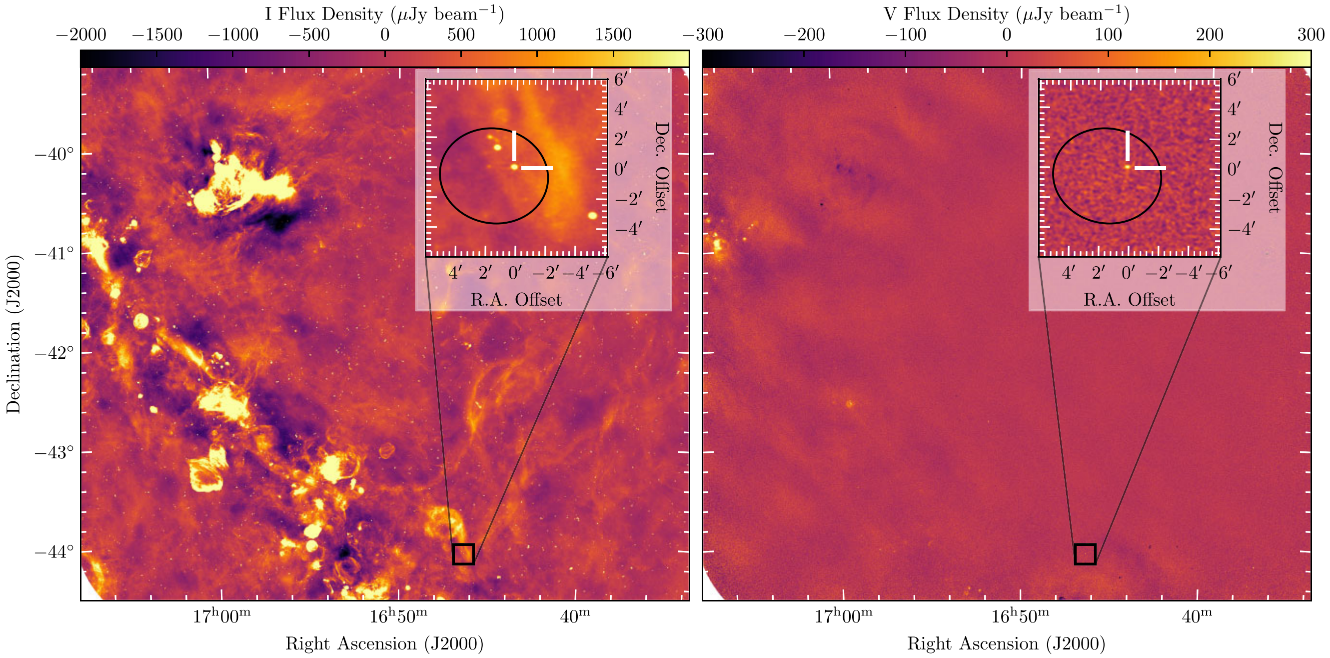

Figure 1. ASKAP field image in Stokes *I* (left) and *V* (right). Inset on both axes is a 6 arcmin × 6 arcmin cutout around ASKAP J1646, where the *Fermi* 95 per cent positional error ellipse around 4FGL J1646 is shown. Note that direction-dependent leakage calibration has not been applied to the Stokes *V* image, so leakage of the order of $\lesssim$1 per cent is visible towards bright, extended regions of emission.

mode, where mass transfer occurs (e.g. Archibald et al. 2009; Roy et al. 2015). There is both theoretical (Benvenuto et al. 2014) and observational (Strader et al. 2019; Clark et al. 2023a) support for the mass of spider pulsars being systematically higher than normal pulsar masses, due to the recent completion of accretion from the donor star, making these systems particularly useful for studies of the neutron star equation of state (Özel & Freire 2016). It also seems apparent that there is an evolutionary link between LMXBs, redbacks, black widows, and field MSPs, but multiple formation mechanisms for redback and black widow systems have been proposed (Chen et al. 2013; Smedley et al. 2015; De Vito, Benvenuto & Horvath 2020; Ginzburg & Quataert 2021). Discovery of new and unusual spiders may provide useful insights into the demographics and formation pathways of these systems (Pan et al. 2023).

The Large Area Telescope on the *Fermi* space telescope (*Fermi*-LAT; Atwood et al. 2009) has enabled a wealth of pulsar discoveries via follow-up of unassociated γ-ray sources. This has included the majority of spider-type systems (e.g. Barr et al. 2013; Bhattacharyya et al. 2013; Camilo et al. 2015; Cromartie et al. 2016; Au et al. 2023; Clark et al. 2023b). There is also growing population of convincing spider candidates (lacking detections of pulses at radio or γ-ray wavelengths) identified by follow-up of *Fermi* sources at X-ray and optical wavelengths (e.g. Strader et al. 2014, 2015; Romani 2015; Braglia et al. 2020; Burdge et al. 2022; Corbet et al. 2022).

Searches for pulsar candidates in radio continuum imaging data sets are also an increasingly successful approach. These include identification of radio sources exhibiting a steep radio spectrum (Backer et al. 1982; Frail et al. 2018; Ray et al. 2022), scintillation (Dai et al. 2016; Dai, Johnston & Hobbs 2017), variability (Wang et al. 2022), high degrees of polarization (Kaplan et al. 2019; Sobey et al. 2022), globular cluster association (Heywood 2023), and association with *Fermi* sources (Frail et al. 2018).

In this paper, we report our analysis and multiwavelength follow-up following new detections of the putative radio counterpart to the γ-ray source 4FGL J1646.5−4406 (hereafter 4FGL J1646). The source was previously investigated by Frail et al. (2018) owing to its positional correspondence with the unassociated *Fermi* source 4FGL J1646, its apparent angular compactness, and its steep radio spectrum – properties consistent with a pulsar origin. However, Frail et al. (2018) determined that it was unlikely to be a pulsar due to a high ratio of its integrated to peak radio flux density, which they proposed to be due to the source being partially resolved. In this work, we revisit the nature of this source after we detected highly polarized emission and periodic radio variability, which we ascribe to the eclipse of a pulsar behind material from a companion. We summarize our unsuccessful search for pulsed emission from this source, but argue that the source is none the less most likely a radio pulsar in a redback binary system. We discuss possible reasons for the non-detection of pulses and place initial constraints on the eclipse mechanism and properties of the eclipsing medium.

2 OBSERVATIONS AND ANALYSIS

2.1 Australian SKA Pathfinder

We detected circularly polarized emission from the radio source ASKAP J164622−440540 (hereafter ASKAP J1646) in an observation taken for the Australian Square Kilometre Array Pathfinder (ASKAP) Evolutionary Map of the Universe (EMU) Pilot Survey (Norris et al. 2021) (Schedule Block ID 28280, observed 2021 June 26).The observations were taken at a central frequency of 943.41 MHz, with 36 beams tiled in a close-pack configuration. The central field coordinates were RA = $16^{h}50^{m}46^{s}$ and Dec. = $-41^{\circ}52'44''$. The data were calibrated using ASKAPSOFT version 1.2.1 and Common Astronomy Software Applications (CASA) version 6.2. Further details on processing and imaging can be found in Norris et al. (2021). We show the observation field in Stokes *I* and *V* in Fig. 1.

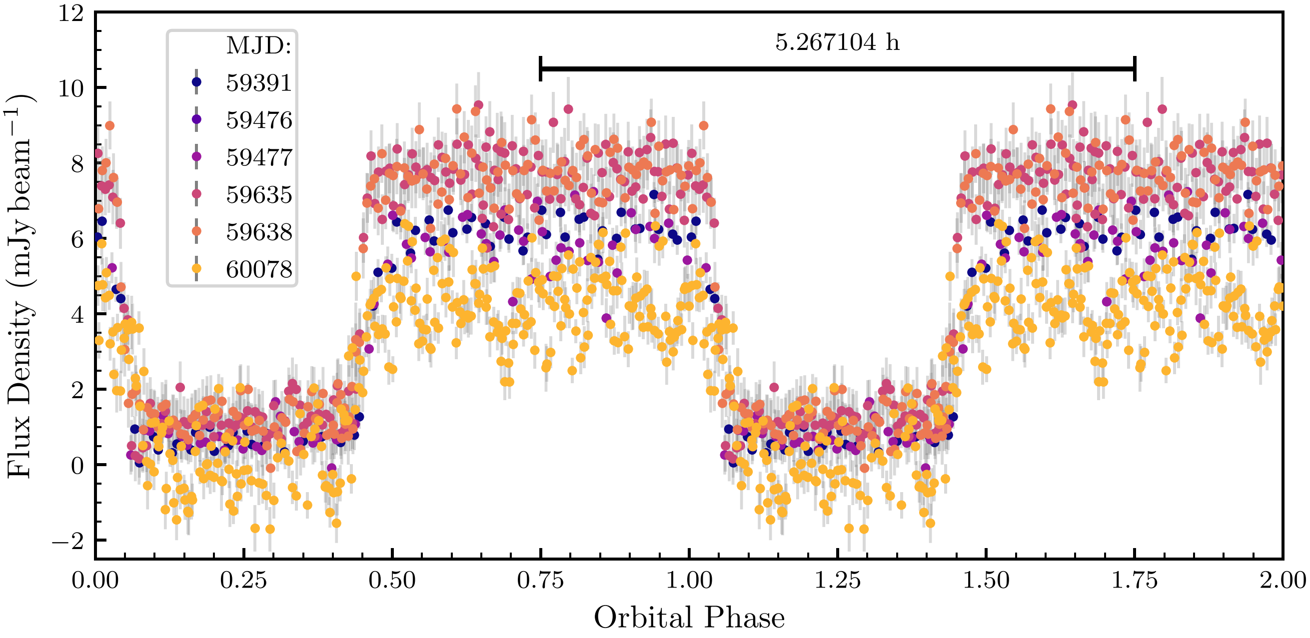

Figure 2. ASKAP radio light curve for ASKAP J1646, folded to the putative orbital period of 5.267 104 h. Points are coloured by their observing epoch. For clarity, we repeat the data from phases 1 to 2 and provide a scale bar to indicate the time span of the orbit. Long-term variability is evident through the differing out-of-eclipse flux densities across different epochs, ranging from ∼4 to 9 mJy.

We detected ASKAP J1646 as a point source in both Stokes *I* and *V*, with flux densities of 5.19 ± 0.06 and $+0.38 \pm 0.03$ mJy, respectively.[1] The resulting polarization fraction $f_c = 7.3 \pm 0.6$ per cent. This is much higher than the typical circular polarization leakage fraction of ~-0.4 per cent in the local region around ASKAP J1646, determined by inspection of nearby bright Stokes *I* sources.

Following the procedure in Zic et al. (2019), we constructed light curves and dynamic spectra for the source by subtracting the sky model constructed during the deconvolution process from the calibrated visibilities. We then phase-rotated the visibilities to the target position and vector-averaged all baselines, yielding complex visibility amplitudes for each correlator integration cycle, frequency channel, and instrumental polarization. We transformed the data from the native instrumental polarization basis (*XX*, *YY*, *XY*, *YX*) into the Stokes basis (*I*, *Q*, *U*, *V*), and produced light curves by averaging the data across frequency.

We found strong, eclipse-like variability in the initial EMU pilot observation, with bright ($S_{943} \sim 7.5$ mJy), stable emission present for approximately 3 h, followed by a period of no detectable emission lasting approximately 2 h. This behaviour was then repeated. In order to confirm the periodic nature of the variability, we conducted further observations with ASKAP on 2021 September 20, 2022 February 25, and 2022 February 28, with identical observing configuration and processing methods to the original EMU pilot observation. After transforming the light-curve timestamps to the frame of the Solar system barycentre, we measured the period by fitting a double Fermi–Dirac function with a freely inferred period and reference epoch (see Section 3.5). This fit yielded a period of $5.267\,104 \pm 3 \times 10^{-6}$ h, with a reference epoch of MJD 59391.3578 ± 0.0005. We show the ASKAP time series from all observations folded at the measured period in Fig. 2.

The apparent non-eclipsed continuum flux density is comparable to measurements reported by Frail et al. (2018). In addition, the strong variability introduces point spread function (PSF) artefacts in the continuum image around ASKAP J1646. These effects may be responsible for the inflated integrated-to-peak flux ratio reported for this radio source in Frail et al. (2018).

2.2 Parkes/Murriyang pulsar search

Motivated by the detection of periodic, eclipse-like variability and circular polarization from ASKAP J1646, along with the spatial coincidence with the γ-ray source 4FGL J1646 (Frail et al. 2018), we carried out pulsar search-mode observations with Parkes 64 m radio telescope, Murriyang, on 2021 September 21 using Director's Discretionary Time (project code: PX080). The observations were carried out with the ultra-wideband low (UWL) receiver (Hobbs et al. 2020), which provides continuous frequency coverage spanning from 704 to 4032 MHz. We coordinated simultaneous observations with the Australia Telescope Compact Array (ATCA; see Section 2.3) to ensure that the emission was present during the pulsar search observations.

We performed a pulsar search using PRESTO, to a maximum dispersion measure (DM) of 1800 pc cm^{-3} [corresponding to a distance >25 kpc based on the YMW16 electron density model (Yao, Manchester & Wang 2017)] and acceleration parameter $z_{\max} = 200$ (corresponding to an orbital period of ∼5.4 h assuming a 3.5 ms spin period and 20 min integration). Since the radio source is quite bright at low frequencies (5.19 mJy at 943 MHz), we split the UWL band into six segments (704–1344, 1344–1856, 1856–2368, 2368–2880, 2880–3520, and 3520–4032 MHz) and searched each segment independently. Searches over the low-frequency segments allowed us to leverage the steep radio spectrum, while searches over the high-frequency segments mitigated potential pulse smearing due to high degrees of scattering (scattering time-scale $\tau_s \sim \nu^{-4}$).

---

[1] In this paper, we use the International Astronomical Union definition of Stokes *V*, where positive (negative) Stokes *V* corresponds to right (left) handed circular polarization.

Table 1. Summary of radio observations.

Telescope	Start (UT)	Δt (h)	ν (MHz)	$\Delta \nu$ (MHz)	Mode	ϕ
ASKAP	2021 June 26 09:22:55	9.9	943	288	Imaging	0–1
ASKAP	2021 Sept 19 19:16:16	1.0	943	288	Imaging	0.59–0.78
ATCA	2021 Sept 21 01:12:55	3.6	2100	2048	Imaging	0.28–0.09
Murriyang	2021 Sept 21 03:41:40	1.0	2368	3328	Pulsar search	0.75–0.94
ASKAP	2021 Sept 20 12:54:53	9.8	943	288	Imaging	0–1
ASKAP	2022 Feb 25 22:24:40	5.5	943	288	Imaging	0–1
MeerKAT	2022 Mar 07 03:39:39	0.67	1284	856	Imaging + Pulsar search	0.69–0.82
MeerKAT	2022 Mar 09 03:01:15	0.67	1284	856	Imaging + Pulsar search	0.68–0.81
MeerKAT	2022 Mar 19 00:00:29	0.67	1284	856	Imaging + Pulsar search	0.68–0.80
MeerKAT	2022 Mar 20 23:24:56	0.67	1284	856	Pulsar search	0.68–0.80
MWA	2022 June 2 to Sept 22	21 × 1.5	200	30	Imaging	0–1

Notes. Δt is the integration time on-source, and $\Delta \nu$ is the total bandwidth around central frequency ν. ϕ is the inferred orbital phase spanned by the observations. For the MWA, we summarize the 21 observations taken from the Galactic Plane Monitoring (GPM) programme used for this source.

After manual inspection of all candidates above a signal-to-noise ratio (S/N) of 4, we did not find any convincing pulsations. We describe further (unsuccessful) pulsar searches with the Meer Karoo Array Telescope (MeerKAT) in Section 2.5 and discuss implications of non-detections in Section 3.

2.3 Australia Telescope Compact Array

We took observations with the ATCA under Director's Discretionary Time (project code: CX489) with the 16 cm receiver. We used the Compact Array Broadband Backend, which delivers ∼2 GHz bandwidth centred at 2.1 GHz. The observations were recorded with 1 MHz channels and a correlator integration time of 10 s. We observed PKS B1934−638 for approximately 10 min for flux density, bandpass, and polarization leakage calibration. We observed ASKAP J1646 in 20 min scans, book-ended between 2 min scans on a nearby gain calibrator, J1646−50. Due to telescope maintenance at the time of observations, antenna CA02 was not available for observing. We flagged and calibrated the data following standard procedures with MIRIAD. Owing to the steep spectrum of the source, we split the 2 GHz band into two 1 GHz segments centred at 1.588 and 2.612 GHz. We used the MIRIAD task MFCLEAN to image each frequency segment. We used a Briggs weighting with a robustness of 0.5, and deconvolved to a depth of 150 μJy, corresponding to approximately 3× the image rms.

We detect the source with a flux density of 1.35 ± 0.06 mJy at 1588 MHz and 0.47 ± 0.06 mJy at 2612 MHz, yielding a spectral index $\alpha = -2.1 \pm 0.25$ ($S_\nu \propto \nu^\alpha$). We constructed light curves by subtracting the sky model generated through deconvolution and self-calibration from the calibrated visibilities using UVMODEL, and fitted the visibilities with a point source model at the location of ASKAP J1646 in 5 and 20 min time intervals. We detected variability in the 20 min light curves at 1588 MHz consistent with eclipse egress near the beginning of the observation (the orbital phase spanned 0.28–0.09), with the source not detected during the first 40 min. However, the S/N and time resolution of the light curves were not high enough for further modelling, and the source was too faint to detect significant variability at 2612 MHz on relevant time-scales.

2.4 MeerKAT imaging

We observed ASKAP J1646 (see Table 1) for 40 min on 2022 March 7, 9, 19, and 20 using the MeerKAT radio telescope at *L* band, with a central frequency of 1.28 GHz (856 MHz bandwidth, 4096 channels) and an integration time of 8 s (project code: DDT-20220227-TM-01). Continuum imaging data were only recorded for observations on March 7, 9, and 19, whereas high time resolution pulsar search data were recorded in all four observations (see Section 2.5). Each observation was scheduled to occur around superior conjunction of the pulsar using an initial eclipse ephemeris derived from ASKAP observations. The resulting continuum images had an rms noise of 20 μJy beam^{-1}. Both interferometric imaging data and pulsar search-mode data were recorded simultaneously in all MeerKAT observations. We used PKS B1934−638 for bandpass and flux density scale calibration, and PKS J1744−5144 for phase calibration. The archived raw visibilities were converted to measurement set format with the KAT Data Access Library (KATDAL)[2] for further continuum imaging. We reduced the data using OXKAT[3] (v0.3; Heywood 2020), where the CASA (McMullin et al. 2007) package and TRICOLOUR[4] (Hugo et al. 2022) were used for measurement sets' splitting, cross-calibration, and flagging; CUBICAL[5] (Kenyon et al. 2018) was used for self-calibration; and WSCLEAN (Offringa et al. 2014) was used for continuum imaging. All processes were executed with OXKAT *L*-band default settings.

We measured peak flux densities of 3.42 ± 0.02 mJy beam^{-1} (March 7), and 3.49 ± 0.03 mJy beam^{-1} (March 19) for ASKAP J1646. The best-fitting position of the source based on the MeerKAT observations is (J2000) $16^{\mathrm{h}}46^{\mathrm{m}}22\overset{\mathrm{s}}{.}75 \pm 0\overset{\mathrm{s}}{.}14$, $-44^{\circ}05'41\overset{''}{.}00 \pm 0\overset{''}{.}14$.

We measured spectral, temporal, and polarization properties for ASKAP J1646 with further reduction on two observations from March 7 and 19. The source had a steep radio spectrum within the bandpass in our MeerKAT observations, with spectral indices $\alpha = -3.1 \pm 0.1$ in both observations. The discrepancy between this measurement and the spectral index reported in Section 2.3 and Frail et al. (2018) may be explained by variability over time-scales of months to years, but we caution that sub-band calibration has not been properly evaluated for our MeerKAT observations, so our measurements may be subject to ∼10 per cent systematic errors.

To check short-time-scale variability, we imaged the target with an integration time of 1 min, which resulted in 40 images for each observation. The light curves showed a relatively low modulation

---

[2] https://github.com/ska-sa/katdal

[3] https://github.com/IanHeywood/oxkat

[4] https://github.com/ska-sa/tricolour

[5] https://github.com/ratt-ru/CubiCal

index (flux density standard deviation divided by the mean) of ~20 per cent and had a reduced χ^2 of 1.4 for 79 degrees of freedom (80 observations minus one parameter for the mean). There was no evidence for minute-scale variability. The fractional circular polarization was ~9 per cent, which was broadly consistent with ASKAP measurements. To search for linearly polarized emission from the source, we split the whole bandwidth into 16 parts (53.5 MHz bandwidth for each part). No linearly polarized emission was detected above the detection threshold (with a 5σ upper limit of 0.1 mJy beam^{-1}) with a maximum accessible rotation measure $|\mathrm{RM}| \lesssim 4000\,\mathrm{rad\,m^{-2}}$.

We also produced dynamic spectra for MeerKAT observations (with the same procedure as that for ASKAP observations, see Section 2.1). There was no evidence of variability beyond the eclipsing behaviour.

2.5 MeerKAT pulsar search

We carried out a periodicity search of ASKAP J1646 using high time resolution pulsar search observations with MeerKAT, recorded with the Pulsar Timing User Supplied Equipment (PTUSE) backend simultaneously with the imaging observations described above.

To account for possible variability in the pulse properties (e.g. in the scattering time-scale), we conducted a periodicity search on 20 min time spans taken from observations on 2022 March 7, 9, 19, and 20 using the full array at *L* band. We divided the data into two sub-bands (856–1284 and 1284–1712 MHz) and searched each sub-band separately using PEASOUP,[6] which is a Graphics Processing Unit (GPU) implementation of a dedispersion and time domain resampling acceleration search algorithm. We used a DM range of up to 1500 pc cm^{-3} [chosen to span all plausible Galactic DMs based on the YMW16 model (Yao et al. 2017)] and spanned an acceleration search range of $|50|\,\mathrm{m\,s^{-2}}$, which is particularly sensitive for detecting circular binary systems with a maximum companion of mass $0.5\,\mathrm{M}_\odot$. The candidates obtained after the search were folded following the methodology outlined in Sengar et al. (2023) before undergoing manual scrutiny. No convincing candidates were found above an S/N of 8. We also repeated the same methodology for the full frequency band, ranging from 856 to 1217 MHz. However, this analysis also yielded no convincing candidates.

The four observations were also independently searched, within the same DM range, with PULSAR_MINER (Ridolfi et al. 2021), an automated pulsar searching pipeline based on PRESTO[7] (Ransom 2001). With the latter, we performed acceleration searches in the Fourier domain using the ACCELSEARCH routine, with a maximum allowed Doppler-induced Fourier bin drift $z_{\max} = \pm 200$. Besides being searched in its full 20 min, each observation was also split into two segments of 10 min, and searched individually, but no splitting of the observing band was made. Similarly to PEASOUP, PULSAR_MINER returned no convincing pulsar-like candidates.

2.6 Murchison Widefield Array

We obtained observations from the GPM programme (project code: G0080) undertaken at 185–215 MHz with the Murchison Widefield Array (MWA; Tingay et al. 2013; Wayth et al. 2018) in 'Phase II extended configuration' in 2022 June to September. The survey covered $|b| < 15^\circ$ and $284^\circ < l < 73^\circ$ using 10×30 min pointings repeated at a cadence of approximately 3–4 d. The survey will be described in full by Hurley-Walker et al. (in preparation). One output of the survey are flux-density and position-calibrated multifrequency-synthesis 5 min snapshot images centred at 200 MHz. ASKAP J1646 lies in the most sensitive part of the main lobe for 30 min per night, and in adjacent pointings for a further 30 min either side, at decreased sensitivity. We used the AEGEAN source finder (Hancock et al. 2012; Hancock, Trott & Hurley-Walker 2018) to measure the flux density at the location of ASKAP J1646 in these images, using the priorized-fit mode, in which the position is fixed and the flux density is fitted (this obtains unbiased estimates when the source is off). The time of measurement was set to the middle of the 5 min integration.[8]

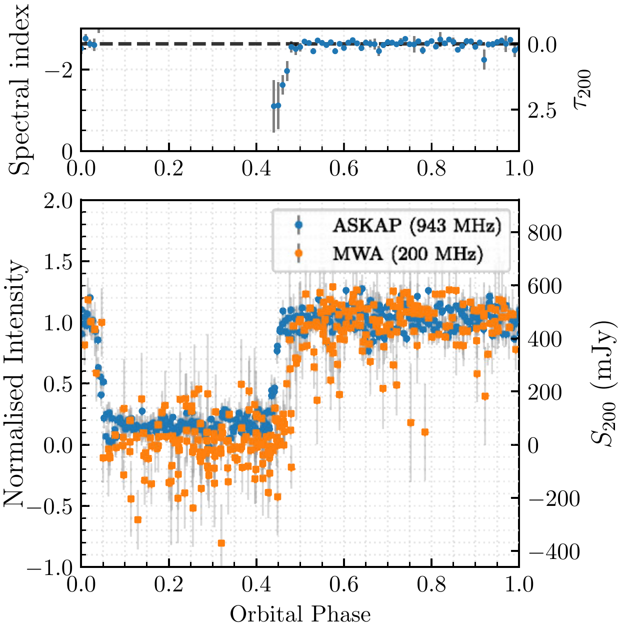

Figure 3. Normalized flux density light curves over orbital phase from ASKAP and MWA observations. The top panel shows the inferred spectral index. On the right-hand axes, we show the inferred 200 MHz optical depth τ_{200} and 200 MHz flux density (S_{200}), respectively. The apparent discrepancy in the eclipse depth between ASKAP and MWA is the result of forced fit for flux density measurements in ASKAP observations, resulting in small but positive flux densities during eclipse when the source is not detected.

In Fig. 3, we show the folded, normalized MWA flux density time series at the period of 5.267 104 h derived from ASKAP observations, which shows similar eclipse-like behaviour as described in Section 2.1 (see Fig. 2). We discuss these eclipses further in Section 3.6.

We also retrieved archival measurements from the MWA Transients Survey (Bell et al. 2019), which was carried out using an earlier, more compact configuration of the MWA. We observed similar eclipse-like variability to that described above, albeit with lower S/N owing to the lower angular resolution. Due to the lower quality of data, we do not consider these observations any further in this paper.

2.7 Archival infrared, optical, and X-ray observations

We searched for archival optical and infrared (IR) observations coincident at the source location. The deepest available observations were from the Vista Variables in the Via Lactea (VVV; Minniti et al.

---

[6] https://github.com/ewanbarr/peasoup

[7] https://github.com/scottransom/presto

[8] While finer time-scale (~4 s) data are available, noise levels of ~60 to −300 mJy beam^{-1} (depending on the pointing) render the S/N too low for detailed measurements of the ingress and egress.

Table 2. AB magnitudes of the possible counterpart to ASKAP J1646.

Filter	λ_{eff} (μm)	$\mathrm{AB}_{\mathrm{mag}}$[a] (mag)
DECaPS *g*	0.480	23.56 ± 0.18
DECaPS *r*	0.638	22.09 ± 0.07
DECaPS *i*	0.777	>22.24
DECaPS *z*	0.911	21.8 ± 0.2
DECaPS *Y*	0.985	>21.1
VVV *Z*	0.878	>23.20
VVV *Y*	1.021	21.13 ± 0.26
VVV *J*	1.254	19.20 ± 0.09[b]
VVV *H*	1.646	20.94 ± 0.28
VVV K_{s}	2.149	20.68 ± 0.32

[a] We report 5σ magnitude lower limits for non-detections.
[b] This measurement is affected by diffraction spikes from a nearby bright star.

2010) in IR and the Dark Energy Camera Plane Survey (DECaPS; Saydjari et al. 2023) in optical wavelengths.

Inspection of archival images from VVV and DECaPS shows an $H \sim 21$ IR source spatially coincident with ASKAP J1646, located at (16$^{\mathrm{h}}$46$^{\mathrm{m}}$22$^{\mathrm{s}}$.74, −44°05′41″.1). The separation between the IR source position and radio source position is 0.12 arcsec – within the astrometric uncertainty of the radio position. The source is also detected in *J* band (1.2 μm), but diffraction spikes from a nearby bright ($J \sim 10$) star make accurate flux measurements challenging. The putative counterpart is also detected in DECaPS in the *g*, *r*, and *z* bands. We provide the detection absolute AB magnitudes in Table 2. In Fig. 4. we show the VVV and DECaPS cutouts overlaid with radio contours of ASKAP J1646. The positional correspondence with the faint optical/IR source is evident. For DECaPS, we computed the false-alarm rates based on the density of sources with *r*-band magnitudes brighter than the putative counterpart within 0.1°, and find rates of $<10^{-3}$ for each epoch. This suggests that the source identified here is indeed the counterpart to ASKAP J1646. The non-detection in VVV *Z* band but detection in DECaPS *z* band is puzzling, but may be due to intrinsic variability from the companion as seen in other spider-type systems (e.g. Draghis et al. 2019). We discuss the nature of the optical/IR source further in Section 3.2.

We retrieved 4.01 ks of archival X-ray observations from the *Swift* X-ray Telescope aboard the *Neils Gehrels Swift Observatory* (Burrows et al. 2005). We merged the individual observations with the online analysis tools.[9] There were two counts within 15 arcsec of ASKAP J1646, but this is consistent with the background. Using a Monte Carlo method by summing counts in independent randomly placed PSF-sized regions across the image (excluding positions of catalogued X-ray sources), we set a 95 per cent upper limit of $7.5 \times 10^{-4}\,\mathrm{s}^{-1}$ in the 0.3–10 keV band. We estimated the upper limit of H I column density for the position of ASKAP J1646 based on the HI4PI survey (HI4PI Collaboration 2016) using the High Energy Astrophysics Science Archive Research Center (HEASARC) web-based NH [10] to be $1.42 \times 10^{22}\,\mathrm{cm}^{-2}$.Assuming a power-law photon index of $\Gamma = 2.0$ (e.g. Lee et al. 2018), we obtain an upper limit on the unabsorbed flux (0.3–10 keV) of $7.6 \times 10^{-14}\,\mathrm{erg\,cm}^{-2}\,\mathrm{s}$ using the HEASARC web-based PIMMS tool.[11]

3 DISCUSSION

3.1 The nature of the source

We have discovered periodic ($P_{\mathrm{b}} = 5.267\,104 \pm 3 \times 10^{-6}$ h, see Section 3.5), eclipse-like radio variability from ASKAP J1646 spatially coincident with the γ-ray source 4FGL J1646. The γ-ray source is offset by 95.2 arcsec at a position angle of 290° from the radio source, well within the *Fermi* positional error ellipse (see Fig. 1). The radio source is point-like, exhibits a steep spectral index ($\alpha \sim -2.7$), and has significant circular polarization ($f_{\mathrm{c}} \sim 7$ per cent). Furthermore, we have identified a potential faint ($g \sim 23.5$, $H \sim 21$) and variable counterpart using archival optical and IR observations.

The only known source class that satisfies this set of characteristics are spider MSP binary systems. In particular, in Section 3.6, we infer an eclipse duration of 0.3994 ± 0.0014 orbits at 943 MHz. The system is therefore most likely a 'redback', which typically exhibits longer eclipses (∼50 per cent of the orbit; Cromartie et al. 2016; Deneva et al. 2021) as opposed to black widows that typically eclipse for ∼10 per cent of the orbit (e.g. Polzin et al. 2020). This is consistent with the higher mass, main-sequence (non-degenerate) companions in redback systems, which are capable of producing larger eclipse regions as the pulsar ablates the companion atmosphere. Based on these insights, we claim that the radio source ASKAP J1646 is associated with the γ-ray source 4FGL J1646, and refer to it as 4FGL J1646 from hereon. Future detection of pulsations in radio and γ-rays would confirm the association.

Multiple spider systems have been previously detected at X-ray wavelengths with redbacks in particular exhibiting relatively high X-ray luminosities around 10^{31} to $10^{32}\,\mathrm{erg\,s}$ (Lee et al. 2018; Zhao & Heinke 2022). Our unabsorbed X-ray flux upper limit of $<7.6 \times 10^{-14}\,\mathrm{erg\,cm}^{-2}\,\mathrm{s}$ implies a luminosity upper limit of $<9 \times 10^{30}\,\mathrm{erg\,s}^{-1}\,(d/1\,\mathrm{kpc})^2$. The X-ray non-detection could therefore be explained if the distance is greater than 1 kpc, although this lower limit estimate is subject to uncertainties around the true hydrogen column density and scatter in the redback X-ray luminosity distribution.

We compiled integral γ-ray fluxes above 100 MeV (E_{100}), radio flux densities (S_ν), along with DMs (where available) for known spider-type binaries using the Australia Telescope National Facility (ATNF) Pulsar Catalogue (Manchester et al. 2005) and the Third *Fermi*-LAT Catalogue of γ-ray Pulsars (hereafter *Fermi* 3PC; Smith et al. 2023).

In Fig. 5 (left panel), we show the ratio of $E_{100}/\nu S_\nu$ versus DM. This quantity, representing the relative flux densities of γ-ray emission to radio emission, is independent of distance, and therefore by proxy is independent of DM. We computed $E_{100}/\nu S_\nu$ for 4FGL J1646, and adopted a lower limit on the DM of $74\,\mathrm{pc\,cm}^{-3}$ (as estimated in Section 3.3) to place 4FGL J1646 in this parameter space. As can be seen, the properties of 4FGL J1646 are consistent with the population of radio- and γ-ray-detected spider binaries.

In Fig. 5 (right panel), we show S_ν as a function of E_{100}, for pulsars in *Fermi* 3PC and for 4FGL J1646. Once again, the parameters of 4FGL J1646 are consistent with the radio-loud population of γ-ray pulsars.

In the following sections, we discuss further constraints on the nature of the system with the available observations.

3.2 Nature of the optical/infrared companion

We show the available optical/IR photometry for the counterpart to 4FGL J1646 in Fig. 6. Note that while VVV and DECaPS both have multiple epochs (and so should allow for variability searches), the

---

[9] https://www.swift.ac.uk/user_objects/
[10] https://heasarc.gsfc.nasa.gov/cgi-bin/Tools/w3nh/w3nh.pl
[11] https://heasarc.gsfc.nasa.gov/cgi-bin/Tools/w3pimms/w3pimms.pl

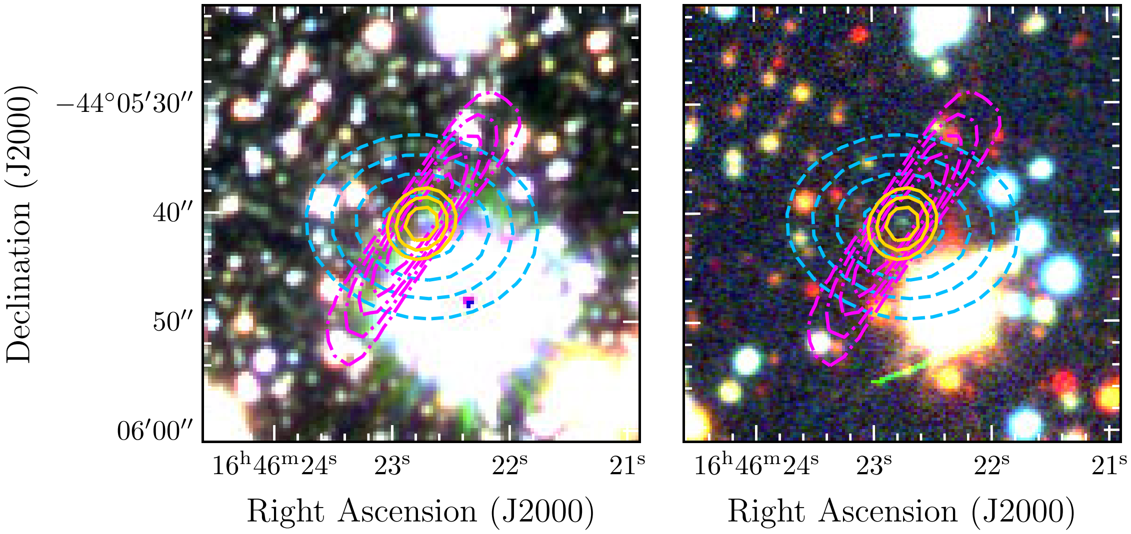

Figure 4. VVV *JHK*s (left) and DECaPS *grz* (right) RGB-coloured cutouts around the position of ASKAP J1646, with radio contours from ASKAP (dashed) and ATCA (dot–dashed) and MeerKAT (solid).

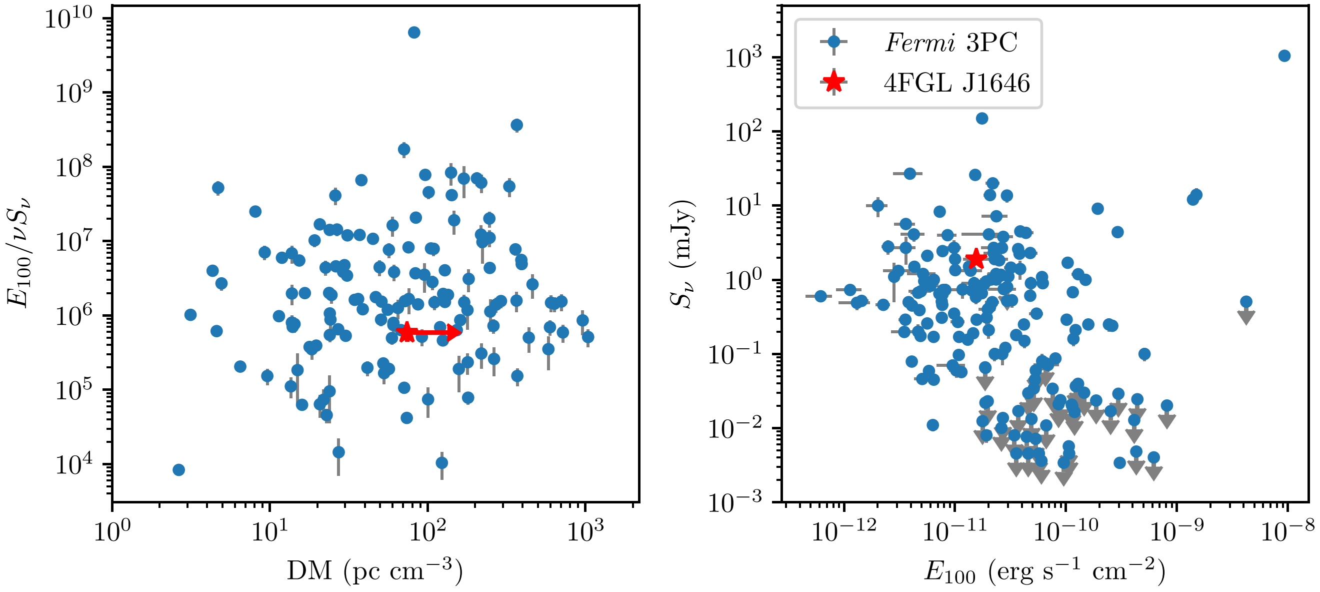

Figure 5. Radio and γ-ray emission properties from the *Fermi* 3PC and for 4FGL J1646. Left: Ratio of E_{100} to νS_ν as a function of pulsar DM. Right: S_ν versus E_{100}. 4FGL J1646 is marked with a star in both panels. The DM lower limit of ∼74 pc cm^{-3} for 4FGL J1646 is derived from scattering properties derived from the NE2001 Galactic electron density model (Cordes & Lazio 2002), based on the estimated DM at which diffractive interstellar scintillation becomes undetectable in our observations. The location of 4FGL J1646 in this parameter space is consistent with the *Fermi* γ-ray pulsar population.

crowded field and marginal nature of some of the detections meant that we were limited to a single average detection for each. As noted above, the data from VVV and DECaPS are not consistent with each other: the source is detected in DECaPS z band but not VVV Z band, with contradictory upper limits. However, many spider systems have significant optical variability from a combination of ellipsoidal modulation and irradiation (e.g. Draghis et al. 2019; Strader et al. 2019; Mata Sánchez et al. 2023). While we do not have sufficient data to do a complete solution of this light curve, we can at least see whether the available data are plausibly fitted by a variable companion to an energetic pulsar.

We assume that the companion has a radius of 50 per cent of the Roche lobe radius (on the small end but consistent with those from Mata Sánchez et al. 2023) at a distance of 3 kpc. We take effective temperatures of 4000 and 10 000 K (again, reasonably consistent with those of the population, although some non-irradiated faces can be significantly cooler). After accounting for an extinction $A_V = 3.4$ mag, we find that the predicted range in flux density is consistent with our observed photometry. This is not a unique solution, but just a plausibility argument: the Roche lobe filling factor and distance are entirely degenerate, and the effective temperatures can also be varied by quite a bit. None the less, we see that the optical/IR emission from the counterpart to 4FGL J1646 does not require an emission region larger than the Roche lobe or an effective temperature much hotter or cooler than other similar sources. Future time-resolved photometry can help establish a more unique solution.

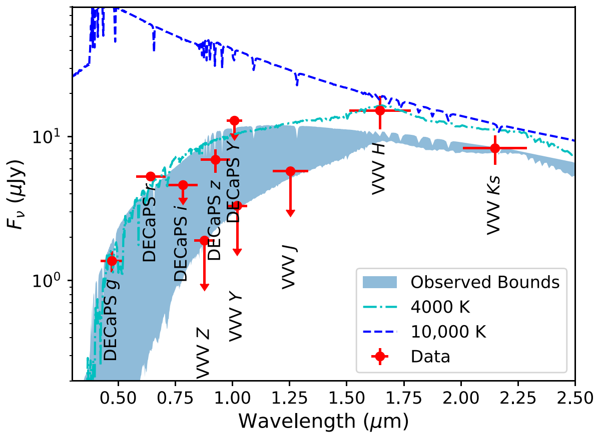

Figure 6. Spectral energy distribution of the optical/IR counterpart to 4FGL J1646. We show the flux densities from VVV and DECaPS (Table 2). We also show model atmospheres from Castelli & Kurucz (2003). We include atmospheres for effective temperatures of 10 000 K (dashed line) and 4000 K (dot–dashed line), roughly bounding the observed range for many spiders. The models are normalized to a radius 50 per cent of the Roche lobe radius and a distance of 3 kpc. These models, with an extinction of $A_V = 3.4$ mag applied are then shown in the shaded region as the observed bounds, which roughly bound the detections and upper limits of the photometry.

3.3 Implications from non-eclipsed radio emission

The lack of significant variability within non-eclipsed time periods in any of our observations implies that the scintillation time-scale or bandwidth is lower than the dynamic spectrum resolution (temporal resolution $\delta_\mathrm{t} = 8$ s and frequency resolution $\delta_\nu = 0.84$ MHz for MeerKAT).

Using this non-detection of scintillation, we can place an approximate lower limit on the DM of ∼74 pc cm^{-3}, using the NE2001 Galactic electron density model (Cordes & Lazio 2002), under the condition that the scintillation bandwidth $\Delta\nu_d < 2\delta_\nu$.

In addition, we can also rule out putative rotation periods exceeding $2\delta_\mathrm{t} = 16$ s. While this is not particularly informative under the spider MSP scenario for 4FGL J1646, it does rule out 4FGL J1646 belonging to the emerging class of recently discovered ultra-long-period objects (Caleb et al. 2022; Hurley-Walker et al. 2022, 2023) or other more unusual radio variables such as Galactic Centre Radio Transient-like sources (Hyman et al. 2005; Wang et al. 2021a).

We also observe long-term variability in the non-eclipsed flux density, as can be seen in Fig. 2. This is typical of spider systems (Polzin et al. 2020; Kumari et al. 2023).

3.4 Non-detection of radio pulsations

Our search for pulsed radio emission from Murriyang and MeerKAT observations yielded no viable candidates. A likely scenario is that the pulses are smeared due to high degrees of scattering from either the intra-binary or interstellar material. In Fig. 7, we show the detectability thresholds for intrinsic pulse duty cycle lower limits as a function of DM for a range of spin periods, owing to scattering in the ISM, using the scattering time-scale–DM relationship from Bhat et al. (2004). At the DM lower limit of 74 pc cm^{-3}, our lack of detected pulsations implies a pulsar-intrinsic duty cycle close to 1, which we consider unlikely. Instead, an interstellar DM exceeding ∼600 pc cm^{-3} would rule out virtually all MSPs from detectability. On the other hand, the scattering may (partially) arise from the intra-binary material, in which case the DM–scattering relationship is less applicable. We discuss this further in Section 3.6.

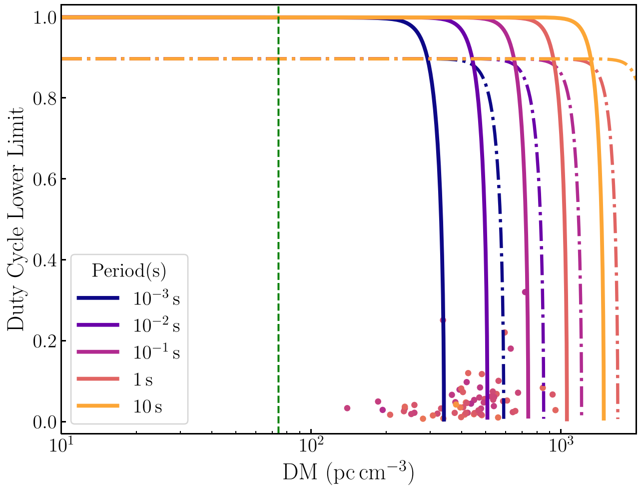

Figure 7. Duty cycle constraints as a function of DM, for a range of pulsar periods. Coloured points show pulsars from the ATNF Pulsar Catalogue (Manchester et al. 2005) within 4° of 4FGL J1646. These pulsars all lie below and to the left of the DM duty cycle locus that defines the boundary of this parameter space where they are detectable, meaning that their pulsations are detectable. Solid lines are the limits derived from the MeerKAT pulsar searches based on the full-bandwidth (856–1217 MHz) data, and dash–dotted lines are the limits derived from the Murriyang UWL pulsar searches based on the top four sub-bands' (3520–4032 MHz) data (expected flux density was derived based on the spectral index from MWA and ASKAP observations, $\alpha = -2.7$).

Alternatively, the lack of radio pulsations could arise from an unusual emission geometry. Typically, spiders are detected with radio and γ-ray pulsations, but some are also radio-quiet (Kong et al. 2012; Corbet et al. 2022). This radio-loud/quiet dichotomy is not fully understood, but it may be due to eclipse phenomena, or geometry of the radio versus γ-ray beam. Here, we have an intermediate case: radio emission, γ-ray emission, but an apparent lack of radio pulsations. While the putative MSP likely produces γ-ray pulses, we did not attempt to search for them due to the excessive computational demands without constrained orbital elements. If the geometry of the system can be constrained by other means (e.g. through optical monitoring or through detection and timing of γ-ray pulsations), this system may provide key insights into the apparent dichotomy between radio-loud and quiet spider binaries, and/or the geometry of MSP emission.

3.5 Derived eclipse properties

The phenomenology of eclipses carries information on the nature of the system and the properties of the intra-binary material (Polzin et al. 2020). To determine the eclipse properties, we fitted the ASKAP and MWA light curves with a double Fermi–Dirac function:

$$\frac{S_\nu(\phi, t)}{S_\mathrm{noncl}(t)} = \beta\left(\frac{1}{\exp\left(\frac{(\phi-\phi_i)}{w_i}\right)+1} - \frac{1}{\exp\left(\frac{(\phi-\phi_e)}{w_e}\right)+1}\right) + (1-\beta), \quad (1)$$

Table 3. Properties of the radio eclipses derived from fitting a Fermi–Dirac function as in equation (1). The spectral index is defined such that the quantity in each row follows a power law, e.g. $\Delta\phi \propto \nu^{\alpha_{\Delta\phi}}$.

Eclipse parameter	MWA (200 MHz)	ASKAP (943 MHz)	Spectral index
P_{b} (h)	–	$5.267\,104 \pm 3 \times 10^{-6}$	
T_0 (MJD)	–	59391.3567 ± 0.0004	
ϕ_i	$0.047^{+0.003}_{-0.007}$	0.0502 ± 0.0016	$0.003^{+0.005}_{-0.003}$
w_i	<0.0064[a]	0.0101 ± 0.0008	$1.2^{+1.1}_{-0.8}$
ϕ_e	0.491 ± 0.002	0.4497 ± 0.0016	-0.121 ± 0.008
w_e	$0.0118^{+0.0013}_{-0.0014}$	0.0089 ± 0.0009	-0.2 ± 0.1
$\Delta\phi$	$0.444^{+0.007}_{-0.003}$	0.3994 ± 0.0014	$-0.069^{+0.005}_{-0.009}$
R_{E}[b]	2.3 $\mathrm{R}_\odot$	2.6 $\mathrm{R}_\odot$	

[a] 90 per cent confidence upper limit. [b] Assuming a companion mass of 0.4 $\mathrm{M}_\odot$.

where $\phi \equiv \frac{(t - T_0)\,\mathrm{per\,cent}\,P_{\mathrm{b}}}{P_{\mathrm{b}}}$ is the derived orbital phase,[12] where t is the MJD time, P_{b} and T_0 are the binary period and reference MJD epoch, respectively,[13] which we allow to vary. Other fitted parameters include $S_{\mathrm{nonecl}}(t)$, the non-eclipsed peak flux density, the ingress and egress phases ϕ_i and ϕ_e, and the $1/e$-width of the ingress and egress, w_i and w_e, respectively. As can be seen in Fig. 2, the non-eclipsed flux density shows substantial long-term variability at 943 MHz. To account for this, we modelled S_{nonecl} as a third-order polynomial in $(t - T_0)$, allowing the polynomial coefficients to vary in the fit.

The constraints on P_{b} and T_0 from MWA measurements were less precise than ASKAP constraints by about an order of magnitude. To ensure consistency between the measured eclipse properties between ASKAP and MWA data, we used a multivariate normal prior on P_{b} and T_0 for fitting MWA data, with the mean and covariance of the prior derived from the ASKAP marginal posteriors. We used uniform priors on all other parameters for both MWA and ASKAP fits.

Using the broad frequency coverage afforded by ASKAP and MWA, we measured the frequency dependence of the eclipse properties parametrized with a power-law spectral index, e.g. $\Delta\phi \propto \nu^{\alpha_{\Delta\phi}}$. We provide the properties in Table 3, along with the derived eclipse radius $R_{\mathrm{E}} = \pi a \Delta\phi$, where a is the semimajor axis assuming a 1.4 $\mathrm{M}_\odot$ pulsar and a companion mass of 0.4 $\mathrm{M}_\odot$ corresponding to typical redback companion masses (Strader et al. 2019).

The inferred eclipse radius is ~2.3 $\mathrm{R}_\odot$, which is ~1.5 times larger than the Roche lobe radius $R_{\mathrm{L}} \sim 1.6$ $\mathrm{R}_\odot$ assuming a pulsar mass of 1.4 $\mathrm{M}_\odot$ and companion mass of 0.4 $\mathrm{M}_\odot$ (computed using the approximation of Eggleton 1983), confirming that the eclipses are due to an unbound cloud of material from the companion. The source of this material could be either the ablated material from the companion and/or the wind from the putative pulsar itself.

3.6 Nature of the radio eclipses

The phenomenology of radio eclipses in spider systems is very broad, considering eclipses both in individual systems and across different systems (Polzin et al. 2019, 2020). Multiple (possibly overlapping) mechanisms have been suggested to drive the eclipses – see e.g. Thompson et al. (1994) for analytical treatment of eclipse mechanisms and Polzin et al. (2020) for an overview of observational results across multiple systems. The eclipse mechanisms may influence the pulse properties (e.g. DM or scattering), and can also absorb the continuum flux density. In the case of 4FGL J1646, we observe 100 per cent absorption of the continuum flux density, but the lack of observed pulsations renders other observables (e.g. change in DM) unattainable.

None the less, our relatively long observational time span from ASKAP and MWA observations, and the broad frequency coverage they afford, enable us to investigate the properties of the eclipse and make some initial estimates of the physical conditions within the eclipse medium.

Following similar arguments to e.g. Kansabanik et al. (2021), we investigated eclipse mechanisms proposed by Thompson et al. (1994): cyclotron absorption, induced Compton scattering, free–free absorption, and synchrotron absorption. Without strong constraints on the properties of the companion or the binary orbit, we can only make broad estimates of the properties of the eclipse medium. None the less, we carry out this exercise to determine whether any eclipse mechanisms can be ruled out and to estimate a plausible range of eclipse medium properties. For the following calculations, we assume a companion mass of 0.4 $\mathrm{M}_\odot$, which is typical for redback systems (Strader et al. 2019), and a pulsar mass of 1.4 $\mathrm{M}_\odot$. The measured period of 0.219 4594 d implies an orbital semimajor axis of ~ 1.9 $\mathrm{R}_\odot$ for the assumed companion mass.

For cyclotron absorption, we estimate the eclipse region magnetic field assuming equilibrium between the wind energy density $U_E = \dot{E}/4\pi c a^2$ and the magnetic pressure $P_B = B_E^2/8\pi$. Assuming $\dot{E} \sim 10^{34}$ erg s^{-1}, we have $U_E \sim 1.6$ erg cm^{-3}, and $B_E \sim 6.3$ G. We find that the required temperature to produce eclipses at 943 MHz is $>4 \times 10^7$ K, which exceeds the 1.7×10^6 K upper threshold for cyclotron absorption (Thompson et al. 1994). We therefore rule it out as the eclipse mechanism.

For induced Compton scattering, we varied the electron column density (between 10^4 and 10^{30} cm^{-2}), temperature (between 10^2 and 10^9 K), and de-magnification factor (between 0 and 1) due to reflection of the radiation off a curved plasma cloud. The maximum optical depth we calculated across the parameter space was $\tau \sim 10^{-2}$, so we therefore rule out induced Compton scattering as the eclipse mechanism.

To determine the viable range of parameters for free–free and synchrotron absorption, we calculated the optical depth for MWA 200 MHz observations just after full eclipse egress at 943 MHz, around orbital phase 0.47 (i.e. when the 943 MHz optical depth τ first returns to 0). The resulting 200 MHz optical depth was $\tau = 2.3 \pm 0.9$. An important caveat for these estimates is that the measurements at the relevant orbital phase were taken several months apart, so long-term variability will introduce a systematic uncertainty of ~10 per cent. Any constraints on the physical properties of the medium should therefore be taken as order-of-magnitude estimates only. To determine the physical properties, we fit the optical depth for free–free and synchrotron absorption using Markov Chain Monte Carlo, fitting to the 943 and 200 MHz flux density at the chosen orbital phase $\phi = 0.47$ during partial egress.

For free–free absorption, we varied the electron column density between 10^{10} and 10^{25} cm^{-2} – a very broad range around typical column densities of ~10^{16} cm^{-2} (e.g. Stappers et al. 1996; Bai et al. 2022). We also allowed the temperature to vary between 10^0 and 10^{10} K, and the clumping factor to vary between 10^0 and 10^{10}. We held the size of the absorbing medium fixed at $2R_{\mathrm{E}} = 4.7$ $\mathrm{R}_\odot$ assuming a 0.4 $\mathrm{M}_\odot$ companion.

---

[12] The symbol '%' is the modulo operator.

[13] Here, we define the reference epoch such that the mid-point of the eclipse, which approximates superior conjunction of the companion, falls at orbital phase 0.25, following the pulsar convention. Note that because we cannot derive a full binary solution, T_0 in our model is likely only an approximation to the epoch of ascending node.

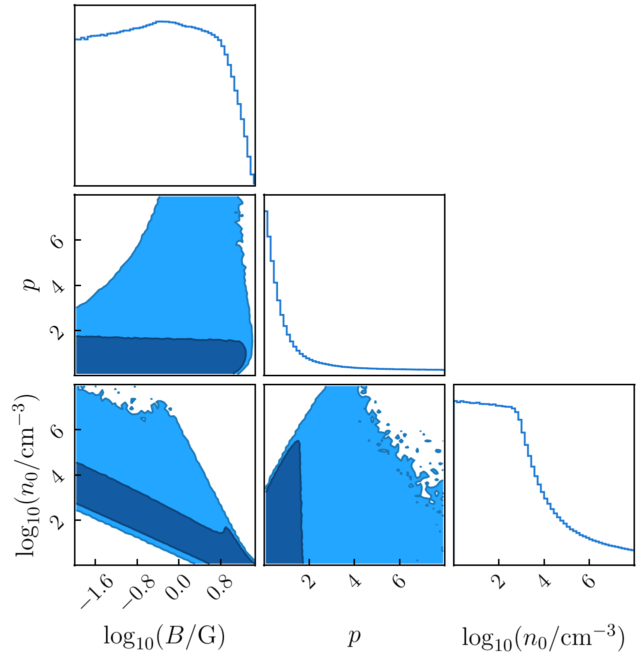

Figure 8. Marginal posterior probability densities of eclipse medium properties (non-thermal electron density n_0, magnetic field strength B, and electron energy power-law index p) assuming synchrotron absorption.

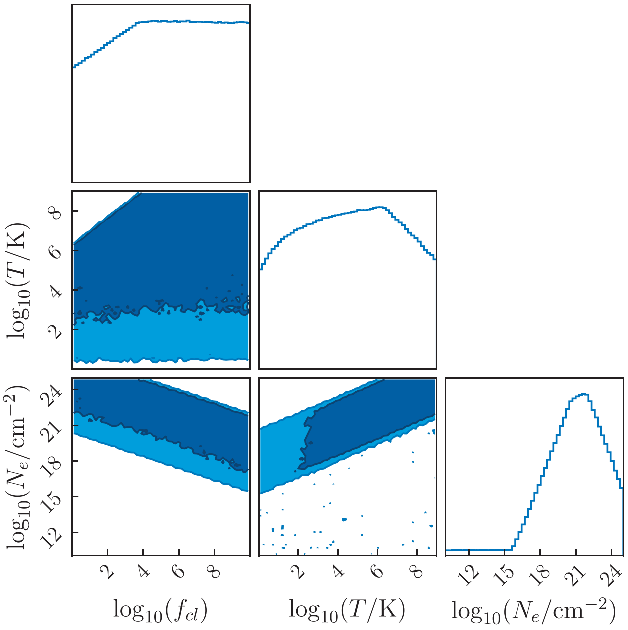

Figure 9. As with Fig. 8, but for eclipse medium properties (clumping factor $f_{\rm cl}$, temperature T, and electron column density $N_{\rm e}$) assuming free–free absorption.

Synchrotron absorption is caused by a population of non-thermal electrons, often assumed to possess a power-law energy distribution $n(E) = n_0 E^{-p}$ between minimum and maximum energies $E_{\rm min}$ and $E_{\rm max}$, respectively (Thompson et al. 1994). We allowed the reference volume density of non-thermal electrons n_0 to vary between 10^1 and $10^8\,\mathrm{cm}^{-3}$, the eclipse average magnetic field strength between 10^{-2} and 10^2 G, and the electron energy power-law index p between 0 and 8. We held the viewing angle θ fixed to $\pi/3$ (corresponding to the expectation value of θ assuming a uniform distribution in $\cos\theta$). As with free–free absorption, we held the size of the absorbing medium fixed at $2R_{\rm E} = 4.7\,\mathrm{R}_\odot$.

Figs 8 and 9 show the marginal posterior probability densities on each of the varied parameters in the synchrotron and free–free absorption models. We found that a broad range of parameters could reproduce the observed optical depths at the relevant orbital phase, but we are able to rule some regions of parameter space out. For instance, if free–free absorption is responsible for the eclipses, then the electron column density must exceed $10^{15}\,\mathrm{cm}^{-2}$. If we assume an equipartition magnetic field strength of $\sim$6 G (as with cyclotron absorption) in the synchrotron-absorbing plasma, then $n_0 \lesssim 100\,\mathrm{cm}^{-3}$. Independent constraints on the eclipse medium density (e.g. from measurements of DM variations near eclipse) will significantly improve constraints on the eclipse medium properties.

Polzin et al. (2020) noted substantial differences in the behaviour of eclipses in the continuum and pulsed flux in a sample of black widows. These differences imply that multiple eclipse mechanisms are operating in at least some spiders – one that absorbs the continuum flux density, and another that reduces the pulsed flux density via temporal smearing. We now explore whether a similar scenario may apply to 4FGL J1646, whereby the continuum flux density is absorbed by e.g. synchrotron absorption, but scattering across a more extended volume in the intra-binary material destroys the pulsed flux density across the full orbit.

We consider an extended scattering eclipse medium with radius $R_{\rm E} = 2a$, such that the pulsar is always enveloped, and its pulsed emission therefore scatter-broadened beyond detectability. Thompson et al. (1994) considered the density fluctuations required to render pulsed emission undetectable due to scattering in a turbulent eclipse medium. The fractional density fluctuations $\Delta n_{\rm e}/n_{\rm e}$ over a length-scale L_n required to broaden a pulse for more than a pulsar spin period P is (Thompson et al. 1994)

$$\frac{\Delta n_{\rm e}}{n_{\rm e}} \gtrsim 7.6\times 10^{-6}\,\frac{\nu_9^2}{n_{\rm e,8}}\,\frac{P_{-3}^{1/2}}{(R_{\rm E,11}a_{11})^{1/2}}\,L_n^{1/2}\,, \qquad (2)$$

where the subscript numerals represent the normalization factor for the various quantities in cgs units, e.g. $n_{\rm e,8} = n_{\rm e}/10^8\,\mathrm{cm}^{-3}$. We show the constraints on the density fluctuations in Fig. 10. For typical densities $n_{\rm e} \sim 10^7\,\mathrm{cm}^{-3}$ and short fluctuation length-scales $L_n \sim 10^3$ cm, fractional density fluctuations of $\sim$$10^{-2}$ to 10^{-1} are required to scatter-broaden the pulses out of detectability. However, the requirements are less stringent at higher mean densities.

Better constraints on the companion and its orbit, along with ultra-wideband continuum observations will enable more precise measurements of the physical properties of the eclipse in future. If the scattering is indeed eclipse-dominated, a dedicated radio observing campaign targeting the period just before eclipse ingress – where the density of the eclipsing material is likely to be lowest – may yield a future detection of radio pulses.

4 CONCLUSIONS

We have presented the discovery of radio eclipses from ASKAP J1646−4406, which we associate with the γ-ray source 4FGL J1646. The radio-frequency and multiwavelength properties strongly suggest that 4FGL J1646 is a spider-type pulsar, most likely a 'redback' with an $\sim$0.4 $\mathrm{M}_\odot$ companion, owing to the long eclipse ($\sim$40 per cent of the orbit). We measure a putative orbital period of 5.267 104 $\pm$ 3 $\times$ 10^{-6}, typical for spider-type systems (Strader

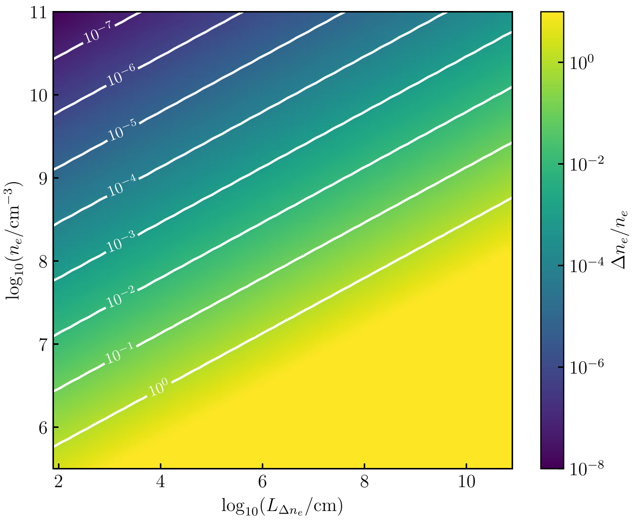

Figure 10. Constraints on the fractional electron density variations $\Delta n_\mathrm{e}/n_\mathrm{e}$ required in the eclipse medium to scatter-broaden pulsed emission beyond detectability in Murriyang observations centred at 3200 MHz, as a function of the mean electron density n_e and the length-scale of density variations L_n. For clarity, we show contours at each decade of $\Delta n_\mathrm{e}/n_\mathrm{e}$ from 1 to 10^{-7}.

et al. 2019). Using the eclipse properties at 943 and 200 MHz, we place broad constraints on plausible eclipse medium properties derived from synchrotron or free–free absorption models, and rule out induced Compton scattering and cyclotron absorption as the eclipse mechanism. Constraints on the electron density of the medium obtained from DM enhancements in pulsed radio emission would greatly improve the constraints on other properties of the eclipse medium.

We searched extensively for radio pulses with Murriyang and MeerKAT, but our searches yielded no convincing pulsar candidates. The non-detection of radio pulses can be explained by temporal smearing due to angular scattering of the emission, from propagation through either the ISM or the eclipse medium. In the ISM case, the lack of pulses can be explained if the interstellar DM exceeds $\sim$600 pc cm^{-3}. If the scattering is dominated by the eclipse medium, a range of turbulent density fluctuations $\Delta n_\mathrm{e}/n_\mathrm{e}$ could smear pulses beyond detectability.

Additional multiwavelength studies for this source are warranted. As discussed in Section 3.2, available optical and IR measurements of the inferred counterpart plausibly agree with the hypothesis of a spider binary, but available data are not sufficient to sufficiently constrain the properties of the system. Future photometric and spectroscopic monitoring of the counterpart across the inferred orbit will be crucial both for confirming the nature of 4FGL J1646 as a redback, and to derive a full orbital solution (Nieder et al. 2020). These orbital constraints will enable a γ-ray pulsation search towards 4FGL J1646, which is computationally infeasible unless the orbital elements are well determined.

ACKNOWLEDGEMENTS

Corresponding authors AZ and ZW contributed equally to this project. We thank the anonymous reviewer whose comments improved this manuscript. Thanks to George Hobbs, Daniel Reardon, and Matthew Kerr for helpful discussions. Thanks to Eddie Schlafly and Andrew Saydjari for help accessing DECaPS data. DLK was supported by National Science Foundation (NSF) grant AST-1816492. RS was supported by NSF grant AST-1816904. NH-W is the recipient of an Australian Research Council Future Fellowship (project number FT190100231). Parts of this research were conducted by the Australian Research Council Centre of Excellence for Gravitational Wave Discovery (OzGrav), project number CE170100004. AR gratefully acknowledges financial support by the research grant 'iPeska' (P.I. Andrea Possenti) funded under the INAF national call Prin-SKA/CTA approved with the Presidential Decree 70/2016, and continuing valuable support from the Max-Planck Society. ASKAP is part of the Australia Telescope National Facility, which is managed by the CSIRO. Operation of ASKAP is funded by the Australian Government with support from the National Collaborative Research Infrastructure Strategy. ASKAP uses the resources of the Pawsey Supercomputing Centre. Establishment of ASKAP, Inyarrimanha Ilgari Bundara, the CSIRO Murchison Radio-astronomy Observatory, and the Pawsey Supercomputing Centre are initiatives of the Australian Government, with support from the Government of Western Australia and the Science and Industry Endowment Fund. We acknowledge the Wajarri Yamatji as the traditional owners of Inyarrimanha Ilgari Bundara, the CSIRO Murchison Radio-astronomy Observatory site, the Wiradjuri people as the traditional owners of the CSIRO Parkes Radio Observatory site, and the Gomeroi people as the traditional owners of the CSIRO Paul Wild Observatory site. Support for the operation of the Murchison Widefield Array is provided by the Australian Government (NCRIS), under a contract to Curtin University administered by Astronomy Australia Limited. Thanks to Australia Telescope National Facility and South African Radio Astronomy Observatory Operations staff for supporting our Director's Discretionary Time observations.

DATA AVAILABILITY

ASKAP data used in this paper can be accessed through the Commonwealth Scientific and Industrial Research Organisation (CSIRO) ASKAP Science Data Archive (CASDA),[14] using the project codes and Schedule Block IDs provided.Murriyang observations can be obtained through the CSIRO Data Access Portal (DAP),[15] and ATCA observations can be obtained from the Australia Telescope Online Archive (ATOA).[16] MeerKAT continuum observations can be obtained from the MeerKAT archive.[17] Other data can be provided upon reasonable request.

REFERENCES

Agazie G. et al., 2023, ApJ, 951, L8
Alpar M. A., Cheng A. F., Ruderman M. A., Shaham J., 1982, Nature, 300, 728
Archibald A. M. et al., 2009, Science, 324, 1411
Atwood W. B. et al., 2009, ApJ, 697, 1071
Au K.-Y. et al., 2023, ApJ, 943, 103
Backer D. C., Kulkarni S. R., Heiles C., Davis M. M., Goss W. M., 1982, Nature, 300, 615
Bai J. T. et al., 2022, MNRAS, 513, 1794
Barr E. D. et al., 2013, MNRAS, 429, 1633
Bell M. E. et al., 2019, MNRAS, 482, 2484
Benvenuto O. G., De Vito M. A., Horvath J. E., 2012, ApJ, 753, L33
Benvenuto O. G., De Vito M. A., Horvath J. E., 2014, ApJ, 786, L7

---

[14] https://data.csiro.au/dap/public/casda/casdaSearch.zul
[15] https://data.csiro.au/domain/atnf
[16] https://atoa.atnf.csiro.au/
[17] https://apps.sarao.ac.za/katpaws/archive-search

Bhat N. D. R., Cordes J. M., Camilo F., Nice D. J., Lorimer D. R., 2004, ApJ, 605, 759

Bhattacharyya B. et al., 2013, ApJ, 773, L12

Braglia C. et al., 2020, MNRAS, 497, 5364

Burdge K. B. et al., 2022, Nature, 605, 41

Burrows D. N. et al., 2005, Space Sci. Rev., 120, 165

Caleb M. et al., 2022, Nat. Astron., 6, 828

Camilo F. et al., 2015, ApJ, 810, 85

Castelli F., Kurucz R. L., 2003, in Piskunov N., Weiss W. W., Gray D. F., eds, Proc. IAU Symp. 210, Modelling of Stellar Atmospheres. Astron. Soc. Pac., San Francisco, p. A20

Chen H.-L., Chen X., Tauris T. M., Han Z., 2013, ApJ, 775, 27

Clark C. J. et al., 2023a, Nat. Astron., 7, 451

Clark C. J. et al., 2023b, MNRAS, 519, 5590

Corbet R. H. D. et al., 2022, ApJ, 935, 2

Cordes J. M., Lazio T. J. W., 2002, preprint (astro-ph/0207156)

Cromartie H. T. et al., 2016, ApJ, 819, 34

Dai S., Johnston S., Bell M. E., Coles W. A., Hobbs G., Ekers R. D., Lenc E., 2016, MNRAS, 462, 3115

Dai S., Johnston S., Hobbs G., 2017, MNRAS, 472, 1458

De Vito M. A., Benvenuto O. G., Horvath J. E., 2020, MNRAS, 493, 2171

Deneva J. S. et al., 2021, ApJ, 909, 6

Draghis P., Romani R. W., Filippenko A. V., Brink T. G., Zheng W., Halpern J. P., Camilo F., 2019, ApJ, 883, 108

Eggleton P. P., 1983, ApJ, 268, 368

EPTA Collaboration, InPTA Collaboration, 2023, A&A, 678, A50

Frail D. A. et al., 2018, MNRAS, 475, 942

Fruchter A. S., Stinebring D. R., Taylor J. H., 1988, Nature, 333, 237

Ginzburg S., Quataert E., 2021, MNRAS, 500, 1592

Hancock P. J., Murphy T., Gaensler B. M., Hopkins A., Curran J. R., 2012, MNRAS, 422, 1812

Hancock P. J., Trott C. M., Hurley-Walker N., 2018, Publ. Astron. Soc. Aust., 35, e011

Heywood I., 2020, Astrophysics Source Code Library, record ascl:2009.003

Heywood I., 2023, MNRAS, 525, L76

HI4PI Collaboration, 2016, A&A, 594, A116

Hobbs G. et al., 2020, Publ. Astron. Soc. Aust., 37, e012

Hugo B. V., Perkins S., Merry B., Mauch T., Smirnov O. M., 2022, in Ruiz J. E., Pierfedereci F., Teuben P., eds, ASP Conf. Ser. Vol. 532, Astronomical Data Analysis Software and Systems XXX. Astron. Soc. Pac., San Francisco, p. 541

Hurley-Walker N. et al., 2022, Nature, 601, 526

Hurley-Walker N. et al., 2023, Nature, 619, 487

Hyman S. D., Lazio T. J. W., Kassim N. E., Ray P. S., Markwardt C. B., Yusef-Zadeh F., 2005, Nature, 434, 50

Kansabanik D., Bhattacharyya B., Roy J., Stappers B., 2021, ApJ, 920, 58

Kaplan D. L. et al., 2019, ApJ, 884, 96

Kenyon J. S., Smirnov O. M., Grobler T. L., Perkins S. J., 2018, MNRAS, 478, 2399

Kong A. K. H. et al., 2012, ApJ, 747, L3

Kramer M. et al., 2021, Phys. Rev. X, 11, 041050

Kumari S., Bhattacharyya B., Kansabanik D., Roy J., 2023, ApJ, 942, 87

Lee J., Hui C. Y., Takata J., Kong A. K. H., Tam P. H. T., Cheng K. S., 2018, ApJ, 864, 23

McMullin J. P., Waters B., Schiebel D., Young W., Golap K., 2007, in Shaw R. A., Hill F., Bell D. J., eds, ASP Conf. Ser. Vol. 376, Astronomical Data Analysis Software and Systems XVI. Astron. Soc. Pac., San Francisco, p. 127

Manchester R. N., Hobbs G. B., Teoh A., Hobbs M., 2005, AJ, 129, 1993

Mata Sánchez D. et al., 2023, MNRAS, 520, 2217

Miller M. C. et al., 2019, ApJ, 887, L24

Minniti D. et al., 2010, New Astron., 15, 433

Nieder L., Allen B., Clark C. J., Pletsch H. J., 2020, ApJ, 901, 156

Norris R. P. et al., 2021, Publ. Astron. Soc. Aust., 38, e046

Offringa A. R. et al., 2014, MNRAS, 444, 606

Özel F., Freire P., 2016, ARA&A, 54, 401

Pan Z. et al., 2023, Nature, 620, 961

Polzin E. J., Breton R. P., Stappers B. W., Bhattacharyya B., Janssen G. H., Osłowski S., Roberts M. S. E., Sobey C., 2019, MNRAS, 490, 889

Polzin E. J., Breton R. P., Bhattacharyya B., Scholte D., Sobey C., Stappers B. W., 2020, MNRAS, 494, 2948

Ransom S. M., 2001, PhD thesis, Harvard University

Ray P. S. et al., 2022, ApJ, 927, 216

Reardon D. J. et al., 2023, ApJ, 951, L6

Ridolfi A. et al., 2021, MNRAS, 504, 1407

Roberts M. S. E., 2013, in van Leeuwen J., ed., Proc. IAU Symp. 291, Neutron Stars and Pulsars: Challenges and Opportunities after 80 years. Cambridge Univ. Press, Cambridge, p. 127

Romani R. W., 2015, ApJ, 812, L24

Roy J. et al., 2015, ApJ, 800, L12

Saydjari A. K. et al., 2023, ApJS, 264, 28

Sengar R. et al., 2023, MNRAS, 522, 1071

Smedley S. L., Tout C. A., Ferrario L., Wickramasinghe D. T., 2015, MNRAS, 446, 2540

Smith D. A. et al., 2023, ApJ, 958, 191

Sobey C. et al., 2022, A&A, 661, A87

Stappers B. W. et al., 1996, ApJ, 465, L119

Strader J., Chomiuk L., Sonbas E., Sokolovsky K., Sand D. J., Moskvitin A. S., Cheung C. C., 2014, ApJ, 788, L27

Strader J., Chomiuk L., Cheung C. C., Salinas R., Peacock M., 2015, ApJ, 813, L26

Strader J. et al., 2019, ApJ, 872, 42

Tauris T. M., van den Heuvel E. P. J., 2006, in Lewin W., van der Klis M., eds, Compact Stellar X-ray Sources, Cambridge Astrophysics Series, Vol. 39. Cambridge Univ. Press, Cambridge, p. 623

Thompson C., Blandford R. D., Evans C. R., Phinney E. S., 1994, ApJ, 422, 304

Tingay S. J. et al., 2013, Publ. Astron. Soc. Aust., 30, e007

Wang Z. et al., 2021a, ApJ, 920, 45

Wang S. Q. et al., 2021b, ApJ, 922, L13

Wang Y. et al., 2022, ApJ, 930, 38

Wayth R. B. et al., 2018, Publ. Astron. Soc. Aust., 35, e033

Xu H. et al., 2023, Res. Astron. Astrophys., 23, 075024

Yao J. M., Manchester R. N., Wang N., 2017, ApJ, 835, 29

Zhao J., Heinke C. O., 2022, MNRAS, 511, 5964

Zic A. et al., 2019, MNRAS, 488, 559

This paper has been typeset from a TEX/LATEX file prepared by the author.